Earth, Planets and Space

FULL PAPER Open Access

On using a double-thin-shell approach and TEC perturbation component to sound night-time mid-latitude E–F coupling

Weizheng Fu[1*], Tatsuhiro Yokoyama[1], Nicholas Ssessanga[2], Mamoru Yamamoto[1] and Peng Liu[1]

Abstract

Observations and theoretical analysis on the night-time mid-latitude ionospheric irregularities support the postulation of frequently coupled E and F regions. In this paper, we attempt at asserting this notion while using total electron content (TEC) measurements. The TECs are from a dense GNSS receiver network over Japan with more than 1200 stations and a mean distance of ~ 25 km between receivers; thus, ideal for analyzing small-scale perturbations in ionospheric electron density. We take an ansatz that mid-latitude night-time plasma instabilities concentrate at E and F layers. Then the integrated three-dimensional density perturbations are parameterized with a double-thin-shell model. At each shell, perturbation components are assumed identical at any point within a given grid block. Two days with events of night-time medium-scale traveling ionospheric disturbances (MSTIDs), but with different amplitudes, were investigated. Results show that the newly developed technique can infer several horizontal characteristics on E–F coupled instabilities; the coexistence of northwest–southeast (NW–SE) aligned irregular structures in E and F regions is evident. Both E- and F-region irregularities share similar propagation parameters, a shred of clear evidence of strong coupling.

Keywords: Global navigation satellite system (GNSS), Total electron content (TEC), Double-thin-shell model, E–F coupling, Sporadic E (Es), Medium-scale traveling ionospheric disturbance (MSTID)

*Correspondence: fu.weizheng.40y@st.kyoto-u.ac.jp

[1] Research Institute for Sustainable Humanosphere, Kyoto University, Uji, Kyoto 611-0011, Japan
Full list of author information is available at the end of the article

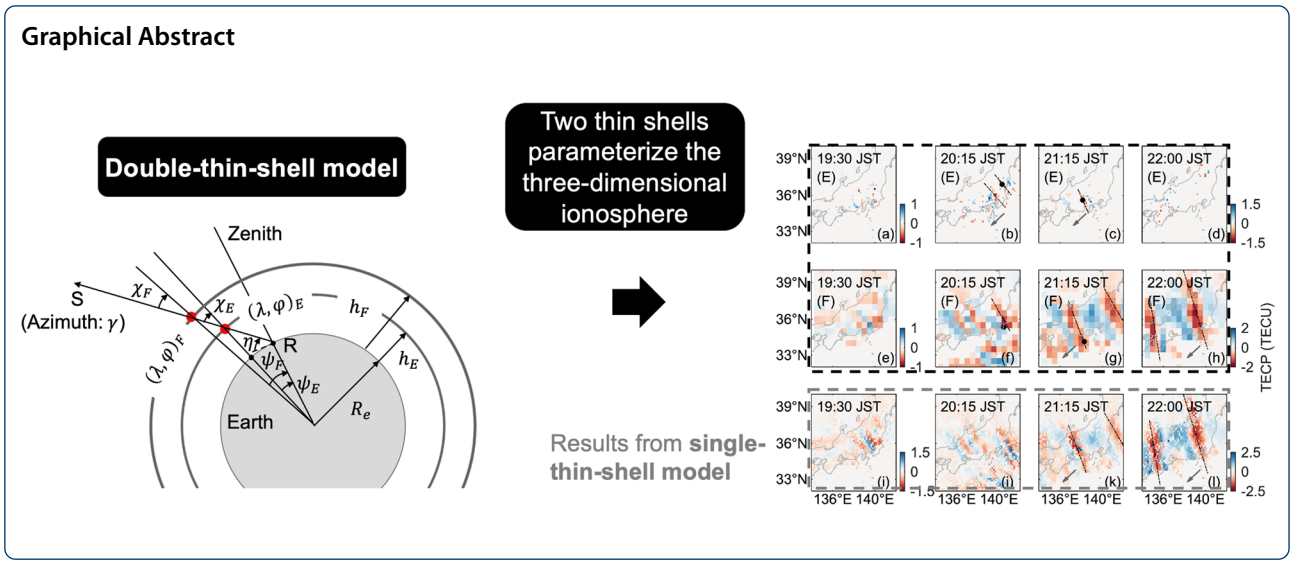

Introduction

The night-time mid-latitude ionosphere is frequently perturbed with two main classes of irregularities: medium-scale travelling ionospheric disturbances (MSTIDs) and sporadic E (Es) (Behnke 1979; Bowman 1985). At frequencies below a few GHz, these irregularities cause signal scintillations which deter navigation and communication systems. MSTID refers to a phenomenon of wave-like plasma density perturbations in the F region, classified by Hunsucker (1982) as traveling ionospheric disturbance with horizontal wavelengths of 100–1000 km. The two-dimensional (2-D) structures of MSTIDs have been studied with the observation instruments such as ionosondes (Berkner and Wells 1934; Bowman 1990), Global Navigation Satellite Systems (GNSSs) (Saito et al. 1998), and airglow images (Shiokawa et al. 2003). At night-time in the Northern Hemisphere, the MSTID structures are preferentially elongated northwest to southeast (NW–SE), propagating southwestward with velocities of approximately 100 m/s (Yokoyama et al. 2009). Sporadic E (Es) are small-scale irregularities that mainly occur in altitude ranging between 95 and 125 km, manifested as thin layers of metallic ion plasma (Whitehead 1989). Observations have inferred that the night-time mid-latitude Es-layer structure is ~ 100 km in length and ~ 10 km in width and propagates southwestward in the Northern Hemisphere (Sinno et al. 1964; Mathews 1998; Maeda and Heki 2015).

Because the shared southwestward preferred propagation direction cannot be explained by the classical theory of atmospheric gravity waves, electrodynamic forces were considered central with the Es-layer instability in the E region and Perkins instability in the F region, as primary generating mechanisms (Yokoyama et al. 2009). Until recently, the two mechanisms were analyzed as a decoupled system (Cosgrove 2013). However, a standalone Perkins instability could not satisfy the instability growth rates in the F-region. Tsunoda and Cosgrove (2001) found that with a positive feedback mechanism under a E–F coupling process, the growth rates were larger than in both independent mechanisms. Different numerical simulations (Cosgrove 2007; Yokoyama et al. 2009), and joint observational experiments (Haldoupis et al. 2003; Otsuka et al. 2007; Saito et al. 2007; Narayanan et al. 2018; Zhou et al. 2018; Liu et al. 2019, 2020; Xie et al. 2020) followed, and confirmed a number of parameters associated with a coupled E–F ionosphere in the night-time midlatitudes. Even with such rich literature, different perspectives still exist regarding the causal relationship in the E–F coupling (Hysell et al. 2018). Moreover, a continuous and broadly spatial distribution of electron densities in the E and F regions is required to deepen our understanding of such an intricate process.

Slant total electron content (TEC) represents the integrated value of electron density along the signal ray path from a transmitter to a receiver and is a vital parameter in the study of ionosphere dynamics. Over a broad frequency spectrum, within which GNSS operate, the ionosphere acts as a dispersive medium that delays the signal propagation and advances the phase: these changes depend on the state of ionosphere plasma density, such that GNSS observables are precise to a certain degree in estimating TEC. To this effect, the cost-effectiveness and rapid development of the GNSS infrastructure, particularly receivers, has effectively broadened the spatial and temporal scales over which ionosphere dynamics are probed. For example, regional to global densely distributed ground-based GNSS receiver networks have enabled the generation of TEC perturbation (TECP) maps to analyze the variation and evolution of ionospheric

disturbances or irregularities: concentric waves and short-period oscillations in the ionosphere (Nishioka et al. 2013), daytime sporadic E (Maeda and Heki 2014, 2015), and MSTIDs (Saito et al. 1998; Otsuka et al. 2008).

At night when Es and MSTIDs simultaneously occur, the use of GNSS TEC to analyze both structures has to date proved challenging. That is to say, the vertical TEC (VTEC) usually used in the analysis is obtained based on a single-thin-shell model, wherein the 3-D ionosphere is represented as an infinitesimally thin layer at a constant altitude. Under such assumptions, high amplitude MSTIDs "shadow" the Es structures with amplitudes generally less than 1 TEC unit ($=10^{16}$ el/m^2). Furthermore, absolute GNSS TEC is mainly estimated to within an accuracy of a few TEC units, hence making a resolve of low amplitude Es densities uncertain. In some cases, where the main plasma density fluctuations or enhancements are located far below or above the F2 peak (e.g., daytime Es), the error in assuming a single shell at F-region altitudes could be disastrous to industry and applications that depend on trans-ionospheric signals.

In response to the above problem, a double-thin-shell model has been proposed as a better approach; for example, Hernández-Pajares et al. (1999) obtained a global ionospheric map based on a two-layer model to reduce the errors inherent to the one-layer model. Shukla et al. (2009) designed a two-shell model, at altitudes 500 km and 300 km, to resolve the Equatorial Ionospheric Anomaly (EIA) density gradients over the Indian region. Maruyama et al. (2021) also parameterized a regional ionosphere that partially encapsulates EIA, with two shells located at high and low altitudes learned from a training data set. In their results, TEC precision was better than in a single-thin-shell approximation, and the EIA was captured adequately. In this paper, we follow the same two-shell model analogy and attempt at sounding the night-time E- and F-region instabilities. Different from Maruyama et al. (2021): (1) The shell altitudes are fixed pre-analysis. (2) Rather than absolute TEC values, we ingest the TEC perturbation (TECP) component. Theoretically, the TECP precision level improves to within 0.01–0.02 TECU, which corresponds to 1% of the wavelength of GPS signals L1 (19 cm) and L2 (24 cm). (3) Analysis is over the Japanese archipelago, which has a dense GNSS receiver network (> 1200 stations with the mean distance of ~ 25 km between receivers) that is ideal in analyzing small density perturbations.

Details of the algorithm and data used in this analysis are presented in section "Data and algorithm" and algorithm validation using observation and simulation is discussed in section "Validation". Results from two MSTID event days are presented and discussed in section "Results and discussion". Section Conclusions gives the conclusions.

Data and algorithm

Black dots in Fig. 1 denote the distribution of GNSS receivers in the dense network. The northeast–southwest (NE–SW) red dashed line in Fig. 1 indicates the region with the most data points. Although most receivers in the network currently track all the signals from available GNSS satellite constellations, the focus here is on GPS. At a data rate of 30 s, every recording is more than 5000 satellite–receiver paths (Saito et al. 1998).

The Slant TEC (STEC), which is the integrated electron density along the line of sight (LOS) between the receiver and satellite, were derived from pseudo-range and phase measurements following the works of Saito et al. (1998) and Ma and Maruyama (2003): phase measurements help in reducing Pseudo-range noise and instrumental biases inherent in the satellites and receivers are assumed to remain stable within one UT day. The TECP component is obtained after deducting a 30-min data running average (centered on the epoch of the LOS) from each LOS TEC. Data corresponding to arc segments less than 30 min are excluded to avoid spurious perturbations. In addition, to mitigate the multipath effects, STEC with elevation angles smaller than 35 degrees were negated. This filtration also reduces the error in the placement of ionospheric piercing points, since such errors are sizeable at low elevation angles.

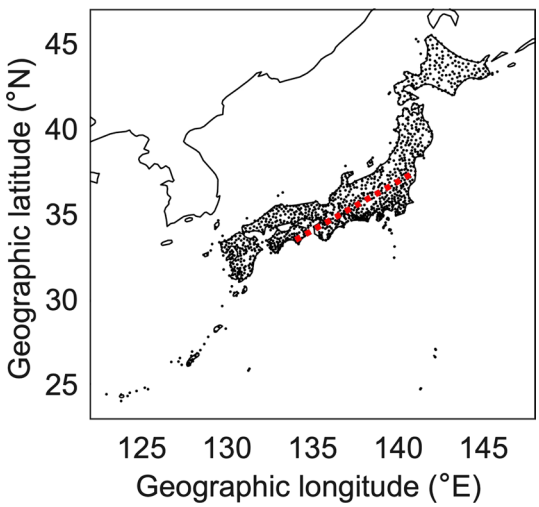

Fig. 1 Distribution of GEONET stations (black dots). The red dashed line indicates the region with most data points

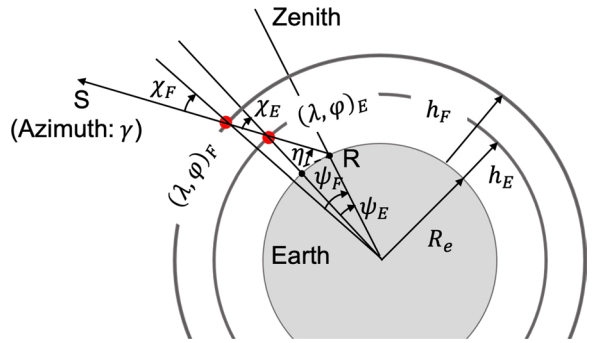

Fig. 2 Typical geometric relation of a GNSS satellite (S) and a receiver (R) in double-thin-shell approximation. η and γ are the elevation and azimuth of the satellite, respectively, χ is the local satellite zenith angle, ψ is the geocentric angle, R_e represents the mean radius of the Earth, h_E and h_F represent the heights of E and F layers, respectively. Red points of intersection (λ, φ) are referred to as the ionosphere pierce points (IPPs)

A typical geometric relation of a GNSS satellite (S) and a receiver (R) in the double-thin-shell approximation is shown in Fig. 2. The slant TECP is assumed to be the summation of the contributions in two thin-shell layers located at two constant heights (E shell and F shell):

$$\mathrm{TECP}^S = \mathrm{TECP}_E^S + \mathrm{TECP}_F^S, \tag{1}$$

TECP^S represents the slant TEC perturbation components from GNSS observations. Although TECP is relatively small, TECP_E^S and TECP_F^S can have large positive and negative values. Even so, the reconstruction of TECP_E^S and TECP_F^S becomes possible if there are a sufficient number of ray paths that cross the reconstruction region at E and F shells. The latitude (λ_i) and longitude (φ_i) of ionosphere pierce point (IPP, shown as red points in Fig. 2), and the local satellite zenith angle (χ_i) in each shell ($i = E, F$ for different shell heights) can be calculated as

$$\lambda_i = \arcsin(\sin\lambda_R \cos\psi_i + \cos\lambda_R \sin\psi_i \sin\gamma), \tag{2}$$

$$\varphi_i = \varphi_R + \arcsin\left(\frac{\sin\psi_i \sin\gamma}{\cos\lambda_i}\right), \tag{3}$$

$$\chi_i = \arcsin\left(\frac{R_e}{R_e + h_i}\cos\eta\right), \tag{4}$$

$$\psi_i = \frac{\pi}{2} - \eta - \chi_i, \tag{5}$$

λ_R and φ_R are the latitude and longitude of the receiver (R), γ and η are the azimuth and elevation angle of the satellite (S), R_e is the mean radius of the Earth, ψ_i is the geocentric angle, and h_i is the shell height. Based on the earlier studies on E- and F-region irregularities (Saito et al. 1998; Maeda and Heki 2015) that utilized ground-based GNSS TEC and a single-thin-shell approach, h_i is set to 100 km and 300 km for the E and F shells, respectively.

Considering the ionospheric irregularities usually occur at altitudes ~ 95–125 km (~ 250–350 km) in E (F) region (Haldoupis et al. 2006; Yang et al. 2015), the maximum uncertainty of the phase front structures manifested in the projections on the ground is about 20 km (45 km), under the double-thin-shell approximation with two constant heights. At a given shell ($i = E, F$), the relationship between vertical TECP (TECP_i^V) and slant TECP is

$$\mathrm{TECP}_i^S = \mathrm{TECP}_i^V / \cos\chi_i. \tag{6}$$

We assumed the ionosphere in the double-thin-shell approximation can be divided into different cells, and the vertical TECPs within a cell in each shell were assumed to be uniform. To make the statistical quantity meaningful, the minimum IPP number inside a cell was set to 3. With all the slant TECPs from GNSS observations, a mixed determined system of the linear equations can be constructed based from Eqs. 1 and 6:

$$\begin{bmatrix} \cdots & \cdots & \cdots & \cdots & \cdots \\ 0 & \sec\chi_{E_{(j-1)k}} & 0 & \sec\chi_{F_{(j-1)k}} & 0 \\ \cdots & \cdots & \cdots & \cdots & \cdots \\ 0 & \sec\chi_{E_{jk}} & 0 & \sec\chi_{F_{jk}} & 0 \\ \cdots & \cdots & \cdots & \cdots & \cdots \\ 0 & \sec\chi_{E_{j(k+1)}} & 0 & \sec\chi_{F_{j(k+1)}} & 0 \\ \cdots & \cdots & \cdots & \cdots & \cdots \end{bmatrix}_{M\times N} \begin{bmatrix} x_1 \\ \cdots \\ x_n \\ \cdots \\ x_N \end{bmatrix}_{N\times 1} = \begin{bmatrix} \cdots \\ \mathrm{TECP}^{S_{(j-1)k}} \\ \cdots \\ \mathrm{TECP}^{S_{jk}} \\ \cdots \\ \mathrm{TECP}^{S_{j(k+1)}} \\ \cdots \end{bmatrix}_{M\times 1} \tag{7}$$

j and k represent the satellite and receiver number, x_n is the unknown vertical TEC perturbation in the n_{th} grid (the E- and F-region unknown densities are compressed into a column vector of N cells) and M is the total number of observations. For convenience, we simplify Eq. 7 to

$$\vec{Y} = \boldsymbol{A}\vec{X} + \vec{E} \tag{8}$$

$\vec{Y}$ and $\vec{E}$ represent observations and errors, respectively, and coefficient matrix $\boldsymbol{A}$ is generally a sparse with columns assumed to be linearly independent. To adequately solve Eq. 8, we use the singular value decomposition (SVD), which has numerically stable properties

and can avoid unrealistic solutions (Ma et al. 2014). If the matrix $\boldsymbol{A}$ is of dimension M and N, then through SVD we can obtain

$$\boldsymbol{A} = \boldsymbol{U}\boldsymbol{D}\boldsymbol{V}^T \tag{9}$$

$\boldsymbol{U} \in \mathbb{R}^{M\times M}$ ($\boldsymbol{V} \in \mathbb{R}^{N\times N}$) is an orthonormal matrix composed of left (right) singular vectors of $\boldsymbol{A}$, associated with singular values or weights contained in a rectangular diagonal matrix $\boldsymbol{D} \in \mathbb{R}^{M\times N}$; T represents matrix transpose. An r-dimensional sub-space of singular vectors is used to represent $\boldsymbol{A} \approx \boldsymbol{U}_r\boldsymbol{D}_r\boldsymbol{V}_r^T$ with a representation of 95% of the total variance, thus the final solution of $\overrightarrow{X}$ can be calculated as

$$\overrightarrow{X} \approx \boldsymbol{V}_r\boldsymbol{D}_r^{-1}\boldsymbol{U}_r^T\overrightarrow{Y} \tag{10}$$

$\boldsymbol{U}\boldsymbol{U}^T = \boldsymbol{I}$ and $\boldsymbol{V}\boldsymbol{V}^T = \boldsymbol{I}$ are used. A more detailed description of SVD and its application to inverse problems can be found in Golub and Van Loan (1989).

Validation

The region to be analyzed covered 30° N–42° N, 130° E–140° E for the E shell and 28° N–45° N, 128° E–145° E for the F shell. For the adequate realization of the instabilities, the resolution in E and F shells was set to 0.15° and 0.5°, respectively. Over a 2.5-min interval, the electron density perturbations were assumed stationary, such that in Eq. 7 $N = 5656$ and $M > 10{,}000$. However, we must take caution that since GPS satellites orbit at altitudes ~ 20,200 km at speeds of ~ 3.8 km/s, depending on the elevation and azimuth angles, the IPP velocities at both E and F shells may sometimes approximate the actual instability phase velocities. In such cases, results are difficult to discern, because the spatial and temporal changes are highly mixed. Fortunately, during the nighttime events analyzed in this paper, the IPP drifts were predominant Northward. Then, with a minimum satellite elevation angle of 35 degrees and a structure at F shell elongated NW–SE and propagating southwestward at ~ 100 m/s, the average estimated error to bear in our analysis was ~ 20% of the actual velocity.

Before analyzing the E–F coupling data set, we addressed two questions to raise confidence in the proposed double-thin-shell model technique: (1) Is the technique able to reconstruct or place the perturbations at the appropriate shell? With disregard to the difference in night and day ionosphere density concentrations, here, as a test case, we analyzed a carefully selected daytime Es event on 21 May 2010 (day of the year (DOY) 141), previously analyzed by Maeda and Heki (2014) and Fu et al. (2021) when the F-region was deemed quiet. The reasoning was that at daytime a well-developed and highly conducting E region limits polarization electric fields that could facilitate the E–F coupling (Kelley, 2009; Fu et al. 2021). Therefore, the signal should be from the E shell, and the F-shell noise dominated. (2) What is the noise threshold below which structures in E and F shells are distinguishable? Because night-time F-shell structures are known to be dominant in amplitude and scale when compared to E-region structures, here, structures were simulated in both E and F regions, and then synthetic STEC were used to analyze the algorithm fidelity when the F-region structure amplitudes and noise level were varied.

An event of daytime sporadic E

Figure 3 shows the horizontal TECP distribution at E- (a–c) and F-shell heights (d–f) of the daytime Es event during 17:00–17:30 JST (Japan Standard Time), on 21 May 2010 (DOY 141). The reconstructed results are consistent with the conclusions obtained in Maeda and Heki (2014) and Fu et al. (2021): at 35° N–36° N, the east–west (E–W) aligned frontal structure of Es is evident in E region during this period; the migration of this frontal structure is southwestward, with a mean speed of ~ 80 m/s; the maximum horizontal scale of this Es structure can reach ~ 350 km in E-W, ~ 30 km in north–south (N–W). To our confidence, the F shell (F region), is noise dominated. Thus, the algorithm can adequately reconstruct the irregularities to the correct shell.

Simulation

A simulation using the real geometry of GNSS satellites and receivers was performed to evaluate and validate this

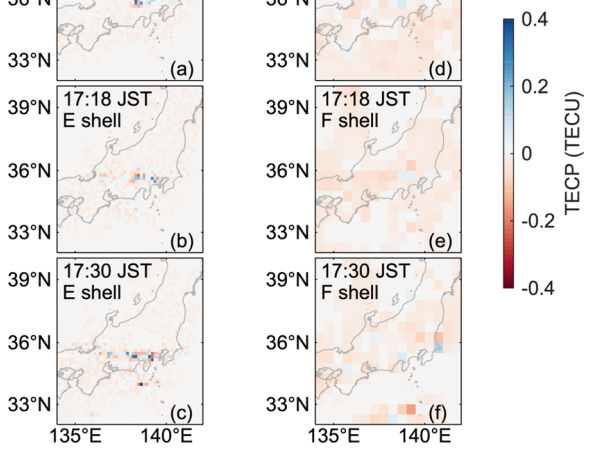

Fig. 3 Snapshots of TECP maps at E- (**a**–**c**) and F-shell (**d**–**f**) heights, at various time epochs from 17:00 to 17:30 JST (Japan Standard Time) on 21 May 2010 (day of the year (DOY) 141)

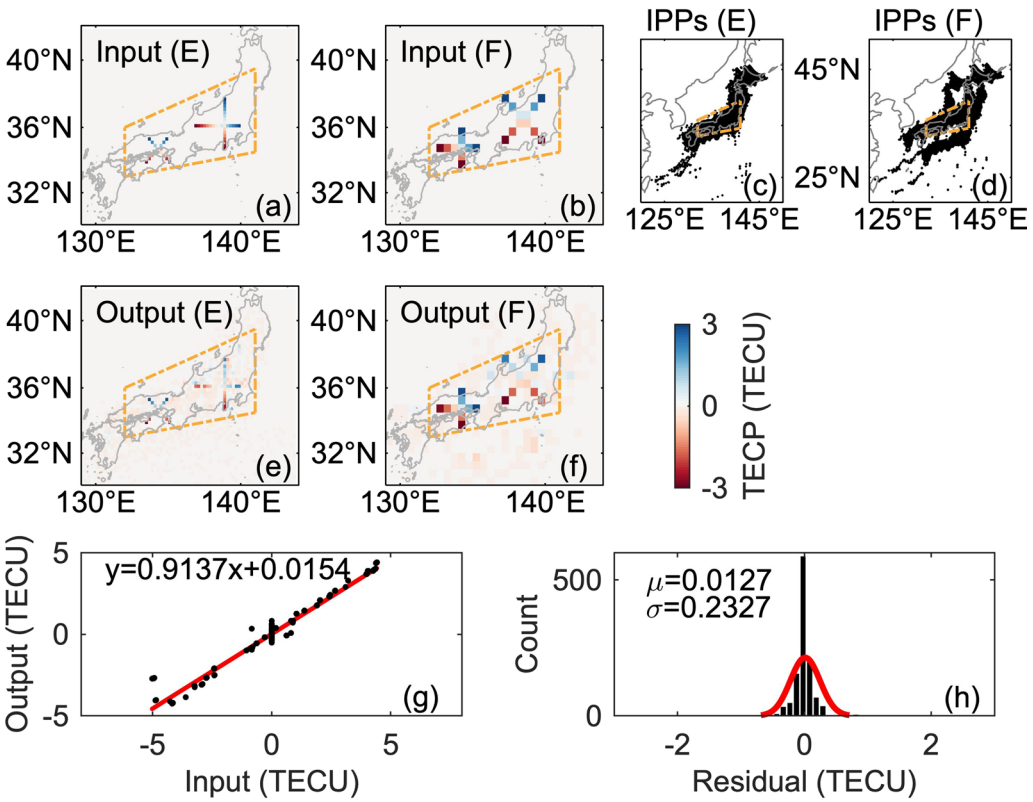

Fig. 4 2-D maps of input (**a**, **b**), IPP distribution (**c**, **d**), output (**e**, **f**) irregularities at E- and F-shell heights, a scatter of input and output total electron content perturbation (TECP) values (**g**) and a distribution of residuals (**h**) using GNSS signal rays at 17:30 JST, on 21 May 2010 (DOY 141). The yellow dashed line indicates a region, where reconstruction is of highest confidence level

algorithm in detail. The 2-D maps of input irregularities at E- and F-shell heights are shown in Fig. 4a, b. Considering the IPP distribution as shown in subplots (c–d), the focus is on the region with dense data points that exhibits high fidelity (bounded with yellow dashed lines in Fig. 4). In the top subplots (a) and (b), two simulated cross irregular structures without noise, but with amplitudes varying within -3–3 TECU (range of most TECPs during MSTID events) were set up in E and F regions. To clearly present the results, the horizontal scales (range of MSTID wavelengths) of input "+" ("x") irregularities were about 250 km (180 km) and 280 km (310 km) in E- and F-shell heights, respectively. About 16,000 real signal rays from GNSS observations at 17:30 JST, on 21 May 2010 (DOY 141) were used. The simulated slant TECPs were then generated as an integral of density perturbations along the ray paths determined from the observation geometry of GNSS satellites and more than 1200 receiver stations from the GEONET. Subplots (e, f) of Fig. 4 show the reconstructed structures: in the area with densely distributed IPPs, the reconstructions at the different shell heights are clearly distinguishable and consistent with the input irregularities in both position and amplitude. Similarly, simulations of two other cases were also analyzed: input irregular structures either in E- or F-shell height. The results are shown in Additional file 1: Fig. S1; the reconstruction still agrees with the input irregularities. In addition, a control data set from 88 GEONET receivers is used to specify the precision. A scatter of input and output TECP values, and a distribution of residuals are plotted in the subplots (g, h). The results suggest a high correlation between input and output values: the gradient to least square fit (red solid line) is 0.91 in subplot (g); the mean (μ) of residuals is 0.01, and the standard deviation (σ) is 0.23 TECU; about 50% of the residuals lie within the first bin (the width of each bin is about 0.1 TECU), and 89% of the data lie within $\mu \pm \sigma$.

To specifically evaluate the algorithm performance in the E region, reconstructions were analyzed under different ratios of E to F region input structure amplitudes (IE/IF). In addition, as stated earlier, the ratios of the standard deviation of noise to F-region input amplitude (N/IF) were also varied. The input irregularities were in the same position as in Fig. 4 (a–b), and the constant input amplitude in the F region was set to 2 TECU (most possible

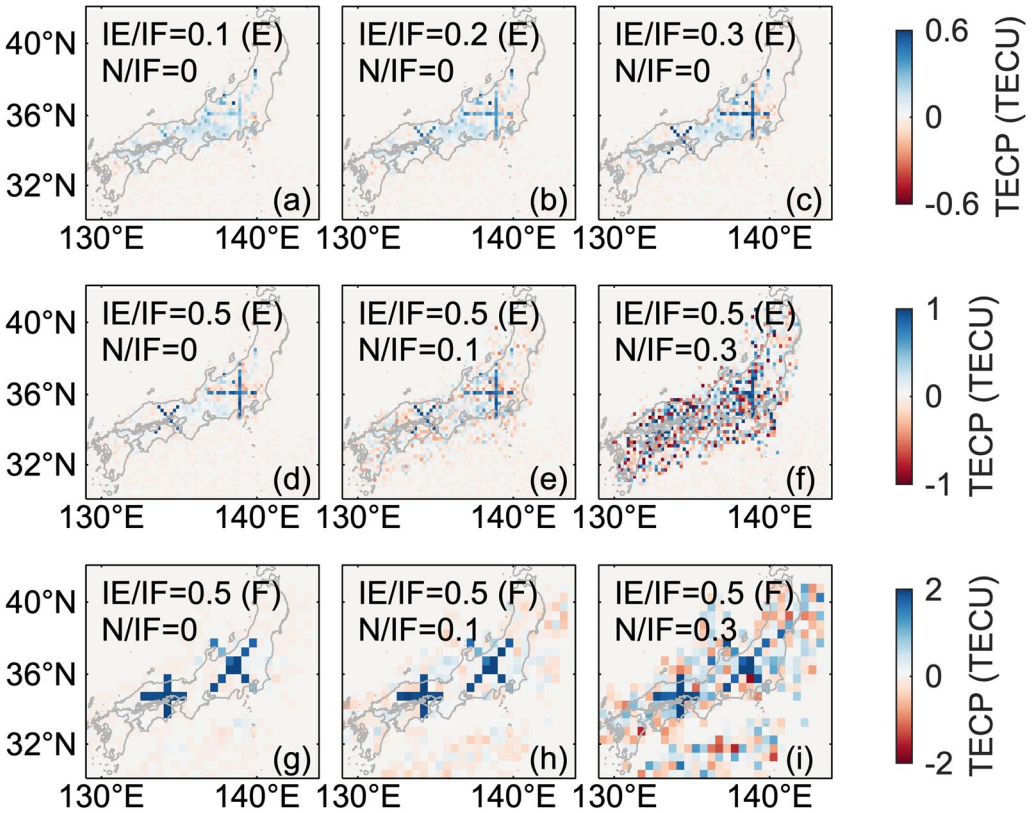

Fig. 5 2-D maps of output irregularities at different ratios of input amplitude in E and F regions (IE/IF) (**a**–**c**), and different ratios of noise standard deviation to input amplitude in F region (N/IF) (**d**–**i**)

amplitude of TECP in MSTID events). In Fig. 5, subplots (a–c) show the reconstructed results in E region with IE/IF = 0.1, 0.2, and 0.3, under the condition of N/IF = 0. In subplots (d–i) IE/IF = 0.5 and N/IF altered. Based on the reconstructed results, even if strong irregularities exist in the F region, E-region irregular structures are well reconstructed when IE/IF ≥ 0.3 and the amplitude of noise not exceeding the amplitude of the E-region irregularities.

Results and discussion

According to the previous statistical studies, night-time MSTID occurrence over Japan maximizes around the June solstice (Shiokawa et al. 2003; Otsuka et al. 2011). A quick look into this period, we selected two night-time events for analysis: 23 June 2012 (DOY 175) and 11 June 2007 (DOY 162). Both days are manifested with MSTIDs, but the amplitudes are different. To mitigate ionospheric disturbances due to other factors such as geomagnetic storms, the ionospheric conditions on the selected events were K < 4 and |Dst| < 30 (Ma et al. 2014). The K index is from data provided by Kakioka magnetic observatory (36.2° N, 140.2° E).

Based on the simulation results in section "Simulation", to reduce the ambiguity of the structures in E shell, reconstructions with IE/IF < 0.3 were excluded. Furthermore, from the work of Fu et al. (2021) that utilized the same geometry, it is better to focus on the region bounded by yellow dashed lines in Fig. 4: most data points are bound to this region. As validation, reconstructions in this region are compared to observations from Kokubunji ionosonde and the middle and upper atmosphere radar (MUR).

Event on DOY 175, 2012

The event on 23 June 2012 (DOY 175) is a typical example of night-time MSTIDs shown in Ssessanga et al. (2017). According to the 2-D TECP maps provided by NICT (National Institute of Information and Communications Technology, in Japan; data accessible at https://aer-nc-web.nict.go.jp/GPS/DRAWING-TEC/), the time period of this strong MSTID event on 23 June 2012 (DOY 175) was from about 11:00 UT (UT = JST-9) to 20:00 UT, and the maximum intensity appeared at around 13:00 UT. Subplots (a–h) in Fig. 6 show the 2-D horizontal

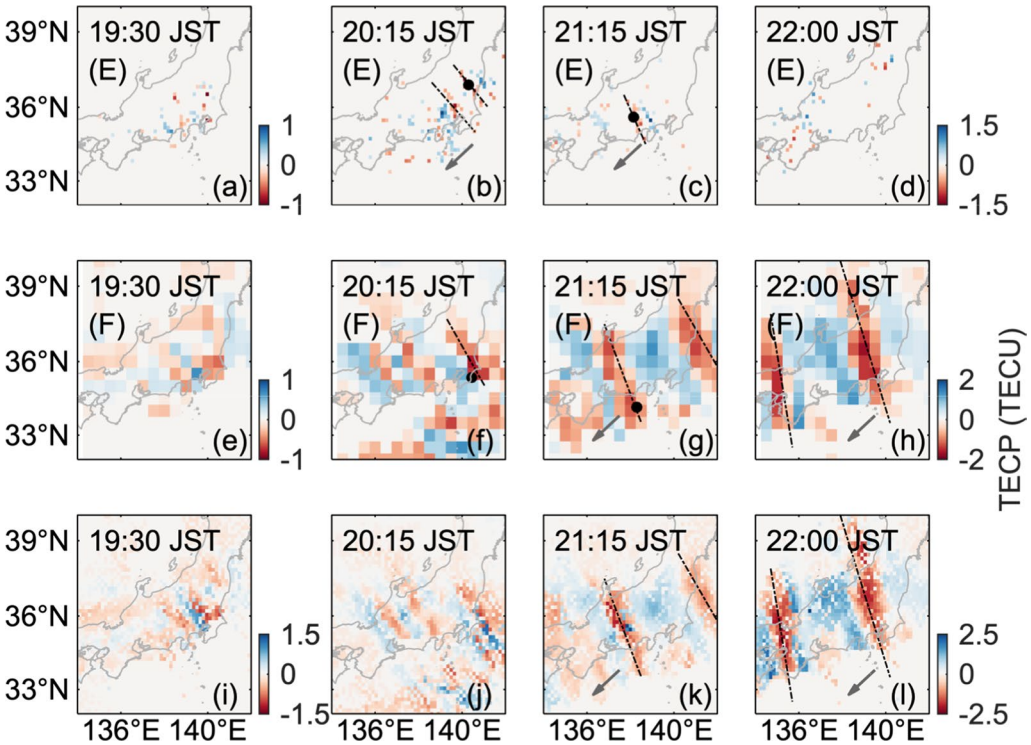

Fig. 6 Snapshots of TECP maps at E- (**a**–**d**) and F-shell heights (**e**–**h**), at various time epochs from 19:30 to 22:00 JST on 23 June 2012 (DOY 175). The subplots in the bottom (**i**–**l**) show the 2-D TECP maps obtained by the single-thin-shell approach. Black dashed lines indicate the alignment azimuth of the apparent frontal structures, gray arrows indicate the drift direction, black dots indicate the locations at E and F shells connected by the geomagnetic field line

TECP distribution maps at E- and F-shell heights under the double-thin-shell approximation, during 19:30–22:00 JST. Bottom subplots (i–l) are the 2-D TECP maps using the same parameters (height: 300 km; grid resolution: 0.15°) as Tsugawa et al. (2018) under the single-thin-shell approximation. Black dashed lines indicate the alignment azimuth of the apparent frontal structures. Gray arrows represent the drift direction (read by eye according to the reconstructed results in a time series). Black dots in subplots b, c, f, and g denote arbitrarily chosen points along the wavefront in the E region (100 km) and the corresponding points in the F region (300 km) following geomagnetic equal potential lines estimated from the International Geomagnetic Reference Field (IGRF) model (Alken et al. 2021). As predicted in the electrodynamic theory of mid-latitude night-time E–F coupling, E and F layer density enhancements/depletions are connected with geomagnetic equal potential lines.

Before 19:30 JST, the E- and F-region irregularities develop but with a small amplitude; probably the early stages of the coupling process. Of course, in this analysis, we cannot pinpoint exactly when instabilities commence, because at the early stages of development, the amplitudes are primarily below the GNSS noise level. After 19:30 JST, the intensity and horizontal scale of E- and F-region irregularities both appear enhanced. Particularly at 20:15 and 21:15 JST, the E- and F-region irregularities migrate southwestward and have preferred NW–SE alignment.

In the top two rows, the average horizontal scales of the E- and F-region irregular structures are about 150 km and 500 km in length and about 30 km and 120 km in width. From the works of Farley (1959), such scale sizes are sufficient for polarization electric fields to map efficiently along magnetic field lines, with coupled E–F regions as a subsequent. A look at both shells, the structures in E and F regions show maximum intensity at around 20:15 and 22:00 JST, respectively, and the F-region structures are well defined than those in the E region: this might be the consequences of the thin layer of Es and the coupling dynamics, wherein the Es layer is easily saturated, and the F-region instability is greatly enhanced in the coupling process, and thus a stronger structuring at the F region. We estimated the center drift phase velocity of the front structures, and the mean migration was about 100 m/s, with a maximum value exceeding 120 m/s. Faster velocities appeared with the rapid development of E-region irregularities. The E- and F-region irregularities

connected by the same geomagnetic field lines had similar propagation parameters. Because these velocities are comparable to observed E-region neutral wind velocities (U_E) (Larsen 2002), we further emphasize the suggestion that the phase velocity of the NW–SE structure in E and F regions is U_E controlled. The theoretical and simulation works of Tsunoda (2006) and Yokoyama et al. (2009) have also underscored the role played by U_E: the E-region rotational wind shear produces southwest phase propagation of the NW–SE structure in both E and F regions even though there is no background electric field, and the NW–SE structures are stationary if the E-region meridional wind is absent. In addition, due to the significant spatiotemporal variation of the E-region neutral wind, the F-region gravity waves may also be a potentially important factor in the propagation of NW–SE structures over a large area in the form of traveling ionospheric disturbances (Yokoyama et al. 2009).

At 22:00 JST, the Es structures were damped out, while the MSTIDs intensified, with two frontal structures exhibiting a spatial wavelength separation of ~200 km. Compared to 20:15 JST, the structures at 22:00 JST are more clockwise, but with the orientation angle more acute at the south most frontal structure. The 3-D E–F coupling simulations by Yokoyama et al. (2009), also insinuated that orientation angle decreases as the magnetic dip angle decreases southward. Indeed, the azimuth and scale of the structures from the double-thin-shell model (subplots g–h) are consistent with the orthodox single shell results (subplots k–l). However, on further analysis, we found a phase difference (less than 50 km) between structures in subplots g–h and subplots k–l: possibly a consequence of utilizing different grid resolutions and the IPP drift error in the two-shell model. Nonetheless, this discrepancy is not large to affect our analysis of the physical underpinnings.

Ionosondes are among the accurate tools for probing the ionospheric plasma density. Here, we consider Kokubunji ionosonde station (located within the region of most GNSS data points in Japan, shown as black triangle in Fig. 7c, d; Ssessanga et al. 2017) observations for validation purposes. Figure 7a–d shows the reconstructed 2-D TECP maps at E-shell height and the Kokubunji ionograms, at 20:15 and 22:15 JST when E- and F-region

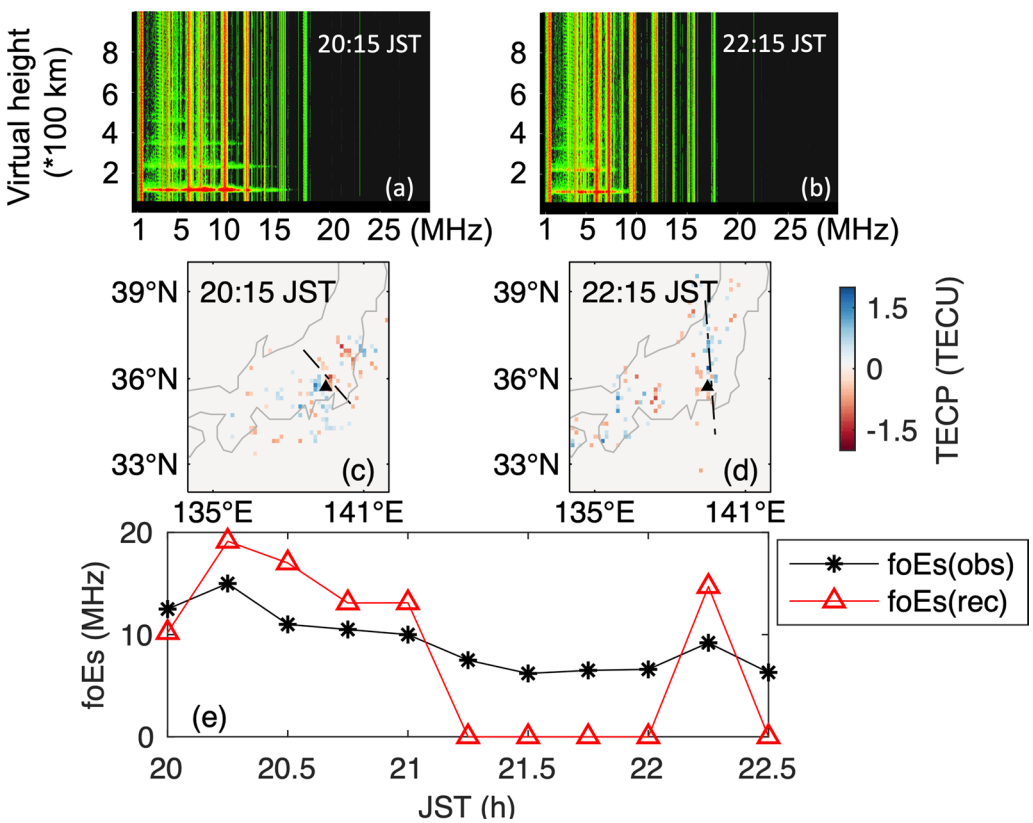

Fig. 7 Ionogram observed by Kokubunji ionosonde (**a**, **b**), and snapshots of TECP maps at E shell height (**c**, **d**) at 20:15 and 22:15 JST on 23 June 2012 (DOY 175). Black triangle represents the location of Kokubunji ionosonde. (**e**) The variation of the *foEs* obtained from ionosonde observations (*foEs*(*obs*)) and reconstructed TECPs (*foEs*(*rec*); a 2 km thickness is assumed) at Kokubunji area during 20:00–22:30 JST

irregularities reach the maximum intensity. Subplot (e) shows the variation of the *foEs* (the critical frequency of Es) obtained from ionosonde observations and reconstructed TECPs (a 2 km thickness is assumed (Maeda and Heki 2014)) at Kokubunji area (a 0.3° grid), from 20:00 to 22:30 JST. During 20:00–22:30 JST, the *foEs* observed by Kokubunji ionosonde reached the maximum amplitude (~ 15 MHz) at around 20:15 JST. The *foEs* decreased and remained at a relatively low level (~ 6 MHz) after 21:00 JST, but had a transient enhancement (~ 10 MHz) at 22:15 JST. The reconstructed results agree with the ionosonde observations: the E-region frontal structure with a high intensity is approaching the Kokubunji area at 20:15 and 22:15 JST; the *foEs* variations obtained by ionosonde observations (*foEs*(*obs*)) and reconstructions (*foEs*(*rec*)) are consistent within 5 MHz. Since reconstructions with IE/IF < 0.3 are excluded and *foEs* are low, the reconstructed TECPs with small amplitude at 21:15–22:00 JST are about zero at Kokubunji area. In addition, the maximum perturbation components of E-region TEC at Kokubunji area are 0.91 TECU (19.16 MHz) and 0.53 TECU (14.62 MHz) at 20:15 and 22:15 JST, respectively, with larger amplitudes but consistent proportions with those of *foEs* assuming a thickness of 2 km. Furthermore, except at 21:15, 21:30 and 22:30 JST when foEs is low, the ionograms clearly reveal the presence of blanketing Es from 19:30 to 24:00 JST as in Fig. 7a, b. That is to say, the radio waves at least up to foF2 cannot penetrate the Es layer, which indicates that the structuring in the Es layer is insignificant (Maruyama et al. 2006).

Figure 8 shows the time variation of E- and F-region TECPs at night-time on 23 June 2012 (DOY 175), with a time resolution of 2.5 min along the line from northeast to southwest indicated as the red dashed line in Fig. 1. H_{eq} represents the equatorial crossing height of the magnetic field line piercing each shell. We consider the irregularities of different shells at the same H_{eq} are related to each other through a magnetic field line. The grid resolution was about 0.3°×0.5° in E- and F-shell heights. The black and gray dashed lines represent the occurrence time of perturbations and the alignment of evident downward-sloping stripes, respectively. For the

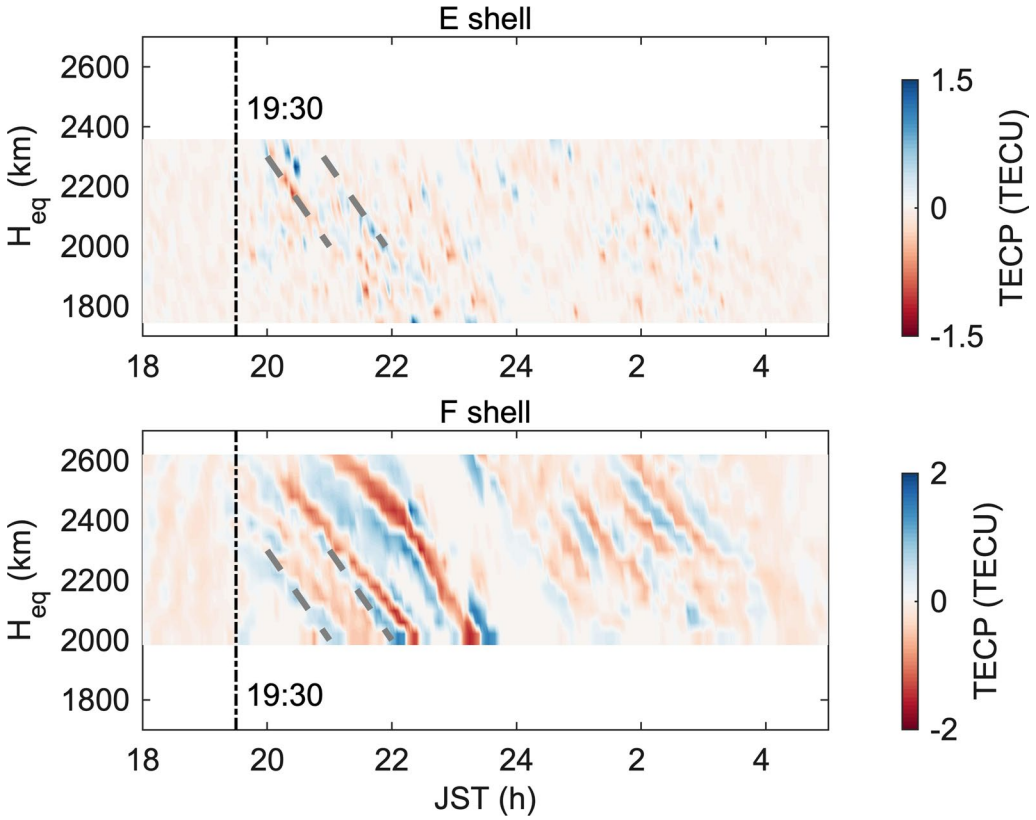

Fig. 8 Time variation of TECPs on 23 June 2012 (DOY 175) along the northeast–southwest red dashed in Fig. 1. H_{eq} is the equatorial crossing height of the magnetic field line piercing each shell. The top and bottom panels represent E- and F-shells, respectively. The black and gray dashed lines represent the occurrence time of perturbations and the alignment of evident downward-sloping stripes, respectively. Evident, particularly between 20:00 ~ 23:59 JST, is the southwestward propagating wavefronts in both E- and F-region

strong post-sunset MSTID event in Fig. 8, the evident downward-sloping stripes at the same H_{eq} indicate irregularities in E and F regions are connected by a magnetic field line and share a similar wavefront with an NW–SE alignment and a southwestward propagation. The occurrence time of the perturbations in E and F regions is almost similar, at ~ 19:30 JST. The maximum amplitude in the E region occurs earlier (~ 20:15 JST) than that in the F region (~ 22:00 JST), but the F-region irregularities show higher intensity. In the later hours of the night, the F-region structures exist in the latitudes and durations when E-region structures are not seen or weak. For the post-midnight MSTID event on 23 June 2012 (DOY 175), the E- and F-region perturbations develop after ~ 0:00 JST and last until ~ 4:00 JST. The Es layer and MSTIDs share a similar amplitude and duration of structure formation but show smaller intensity than the pre-midnight event.

Event on DOY 162, 2007

Since the mid-latitude field-aligned irregularity (FAI) in E region is considered associated with the horizontal inhomogeneity of an Es layer (Larsen 2000; Maruyama et al. 2006), the structured coherent backscatter radar echoes, so-called quasi-periodic (QP) echoes, are associated with Es layers and usually used to indicate the Es dynamics and morphology (Yamamoto et al. 1994; Maruyama et al. 2000; Saito et al. 2007; Xie et al. 2020). MUR, located at 34.9° N, 136.1° E, Shigaraki, Japan, has been used for detecting backscatter echoes from plasma irregularities in both E region (Yamamoto et al. 1994) and F region (Saito et al. 2002). For this event, we used the observations from MUR to further validate our results. Three transmission beams pointing nearly to the geographic north (azimuth angle: − 13.92°–17.67° about the geography north, zenith angle: 51.09°–59.01°) are selected.

The horizontal TECP distribution maps at E- and F-shell heights during 19:00–23:00 JST, on 11 June 2007 (DOY 162), are shown in Fig. 9. Black dashed and gray arrows and black dots represent the same as in Fig. 6. Black stars denote the location of MUR, and the black crosses indicate an example of a regions, where the radar beam intersects the ionosphere at 100 km (E shell) and 300 km (F shell). The transmission beam was pointed to the geographic north (azimuth: 0°, zenith: 52.07° and 57.84° in E and F regions, respectively).

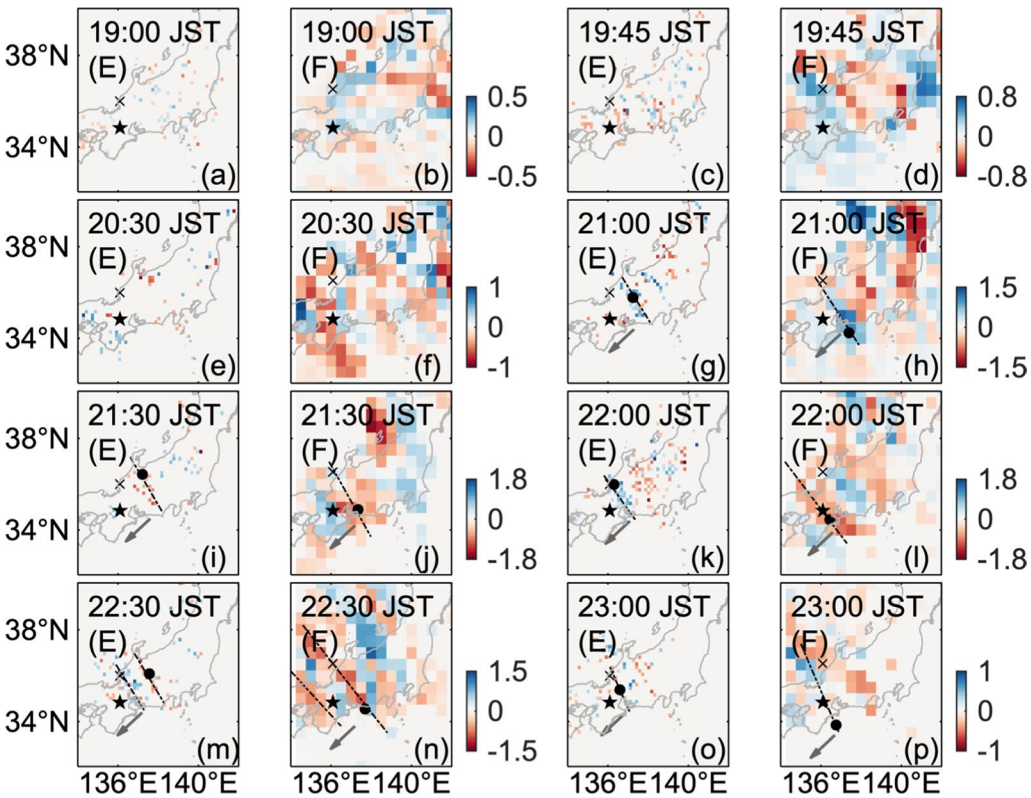

Fig. 9 Same as Fig. 6 but for 11 June 2007 (DOY 162). Black stars are the location of MUR, black crosses represent the observation regions with an altitude of 100 km (E region) and 300 km (F region), where the transmission beam was pointed to the north (azimuth: 0°, zenith: 52.07° and 57.84° in E and F regions, respectively), black dots indicate denote the locations at E (100 km) and F shells (300 km) connected by a geomagnetic field line

Compared to the results in Fig. 6, E-region irregularities in Fig. 9 (before 22:00 JST) are similar in size, but E- and F-region maximum amplitudes (in areas with dense data points) are less by approximately 20%. In Fig. 9, the duration of structure formation in E and F regions are similar: the E- and F-region irregularities both appear enhanced at ∼19:00 JST, and reach the maximum amplitude at around 21:30–22:00 JST. The irregular structures in E and F regions share a common southwestward migration and a similar NW–SE wavefront. The irregularities in E and F regions, which share similar propagation parameters, are considered connected by a same geomagnetic field line, as shown by the frontal structures in the subplots during 21:00–23:00 JST.

Worth noting is that the F-region structures in Fig. 6 depict a longer wavelength and larger amplitude and are well defined than structures in Fig. 9. This result supports 3-D simulations of F-region Perkins instability in Yokoyama et al. (2008): structures showed a wavelength dependence with shorter perturbations tending to saturate at low amplitudes. We also presume that the density perturbations in Fig. 9 dominate at altitudes lower than 300 km. Consequently, the reconstructions are poor due to the increased error in IPP spatial distribution. A strengthened mid-latitude Northern Hemisphere poleward wind could have forced the plasma downwards such that the instability structuring and amplitudes are limited. That is to say, from the theory of a coupled E–F region (Tsunoda 2006), the duration of structure formation and structuring of the instabilities depend on the ratio of field-line-integrated Hall conductivity to Pedersen conductivity (which is proportional to ion-neutral collision frequency, ν_{in}). However, at lower altitudes, ν_{in} is expected to increase and background plasma densities to decrease exponentially due to enhanced recombination rates. Besides, ν_{in} is inversely proportional to the F instability polarization electric fields. This has been shown to be the case observationally in Narayanan et al. (2014).

Since the size of the irregularities measured by the radar backscatter may be several meters, while that detected by the GNSS–TEC measurements is on an order of ten to hundred kilometers, strong backscatter signals and km-scale density enhancement/depletion to a certain extent may not depict an exact direct relationship. Still, from the general relative change in density, and an assumption that meter-scale structures populate a wider spatial area than the radar field of view, we can obtain several important physical underpinnings based

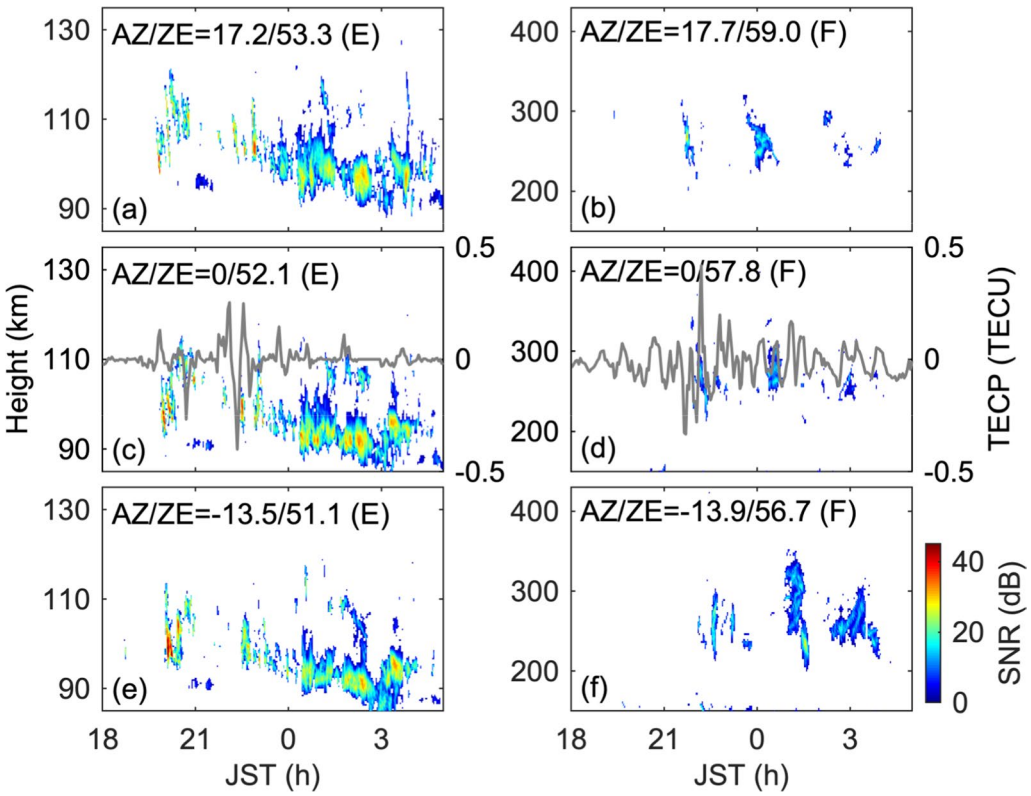

Fig. 10 Range-time-intensity plots of echo power observed with the MUR on 11 June 2007 (DOY 162). AZ and ZE represent azimuth and zenith of the transmission beams, respectively, the gray solid lines represent the mean variation of TECPs in the radar observation regions

on these results and validate the algorithm to a certain extent. Figure 10 shows the range-time-intensity (RTI) maps of echo power observed by MUR on the night of 11 June 2007 (DOY 162), where AZ and ZE represent the azimuth and zenith angles of the transmission beams, respectively. Negative (positive) azimuth corresponds to west (East). In each subplot, the region in observation (E or F) is indicated in parentheses. Gray solid lines in middle panels are the mean variation of TECPs within a 0.6°×0.15° (2°×0.5°) grid covering the radar observation regions at E (F) shell height. According to the E-region RTI subplots, the eastern most beam (AZ=17.2°) detected the echoes first (~20:00 JST) and then followed by other beams. Therefore, movement must have been westward. The inclined striation pattern indicates the occurrence of well-defined QP echoes during ~19:30–24:00 JST, with a period of about 10 min. Besides, continuous echoes associated with lower altitude are observed after ~ 24:00 JST. In the F region, the weak echoes are received from ~ 21:00 to ~ 4:00 JST, and evident irregularities are observed at around 22:00, 1:00, and 3:00 JST with a reduced amplitude. According to the observations of Doppler velocity, the antennas facing further northeast can receive the intense echoes faster, and the Doppler velocity observed by MUR is negative when the first QP echoes were received (~20:00 JST), which indicate that the E-region irregularities in the echoing region are moving southwestward. The echo strength: particularly observations by radar beam (AZ/ZE −13.5°/51.1°), between ~ 18 and 24 JST, the echo is "short-lived" but with a stronger SNR (signal-to-noise ratio). On the other hand, between ~ 00 and 06 JST, echoes are frequent but with a slight reduction in SNR and a descent in altitude. During the later period, the TEC component shows a quasi-quiet variation; we think, due to plasma density reduction following the altitude descent, the integrated density variations are below the TEC noise level.

Saito et al. (2007) has identified that the horizontal scale of QP echoes is about a few tens of kilometers and is much smaller than those in the F-region MSTIDs. In Fig. 10 subplot (c), the occurrence time of E-region irregularities observed by GNSS TEC (~20:00, 22:00, and 23:30 JST) is consistent with that of QP echoes observed by MUR, and the fluctuation of TECPs becomes small after 24:00 JST when continuous echoes were observed by MUR. The continuous echoes are less dynamic than the QP echoes, indicating a development of weak spatial structuring in electron density within an Es layer (Maruyama et al. 2006). The average of absolute E-shell TECPs peak amplitude, where the QP echoes are intense (e.g., ~20:00, 22:00, and 23:30 JST) is ~ 0.3 TECU, which translates to ~ 11 MHz if a 2 km thickness is assumed; this frequency is above a *foEs* threshold above which QP echoes are generally detected in ionosonde observations over Japan (Mungufeni et al. 2021). Despite the consistent, a slight time delay is noticeable in the expected alignment of TECP depletions (negative) and QP echoes: this might be due to the errors in IPP spatial distribution. In addition, "x" is the point, where the beam intersects the 100 km layer, but not the actual echo points, where magnetic fields are perpendicular to the MUR beam.

In the subplot (d), the F-region FAIs are plotted together with F-shell perturbations from the point indicated by "x" in Fig. 9, where the radar beam is projected to pierce the F shell at 300 km. Evidently, at around 22:00 JST, the largest undulations in GNSS–TEC coincide with intense echo stratifications in the MUR observations. However, not all undulations are accompanied by FAIs, probably due to low amplitudes or out of view of the radar beam. Saito et al. (2002, 2008) and Otsuka et al. (2009) and references therein have also shown a summer night-time common occurrence of MSTIDs and FAIs over Japan, and the occurrence of FAIs is related to the intensity of MSTIDs.

Same as Fig. 8 but for 11 June 2007 (DOY 162), Fig. 11 shows the time variation of E- and F-region TECPs in H_{eq} at night-time, along the line from northeast to southwest indicated as the red dashed line in Fig. 1. The black and gray dashed lines represent the occurrence time of perturbations and the alignment of evident downward-sloping stripes, respectively. For this event, the E- and F-region irregularities are of similar duration of structure formation and intensity, but the occurrence time of the downward-sloping stripes is about 10 min earlier in the E region than in the F region. During ~19:30–23:00 JST when QP echoes were obvious in the MUR observation, the evident downward-sloping stripes indicate the E- and F-region irregularities share a similar wavefront with an NW–SE alignment and a southwestward propagation with a phase velocity of 80–150 m/s. The clear inclined striations at ~ 21:00–22:00 JST at the same H_{eq} indicate the E- and F-region irregularities are related to each other through a magnetic field line. During ~24:00–4:00 JST when radar continuous echoes (a lower height and weaker power in the echoing region (Maruyama et al. 2006)) were observed, the E- and F-region irregularities show a reduced amplitude and remain at a lower level (~0.5 TECU). Similar to the results in Fig. 8, the duration of large-intensity downward-sloping stripes (~1 TECU) is longer in the F region (from ~21:00 to 2:00 JST) than in the E region (from ~21:00 to 24:00 JST). This indicates that once formed the F-region structures can sustain longer, which corroborates the observations made by Narayanan et al. (2018).

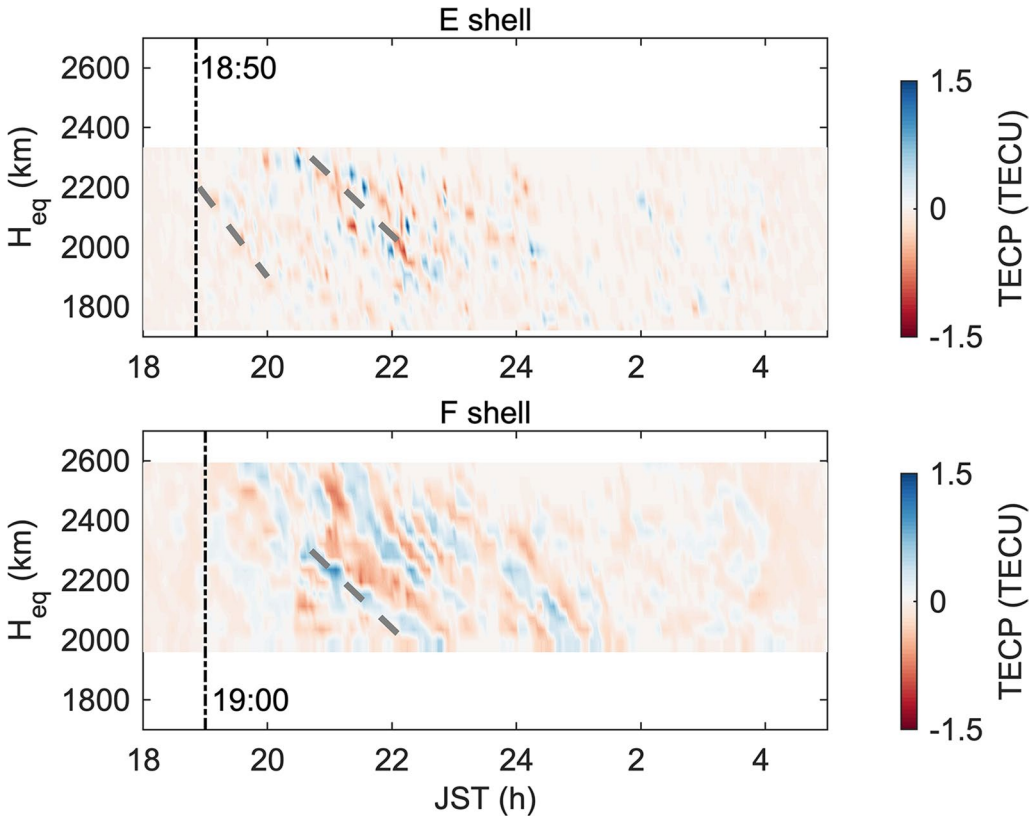

Fig. 11 Time variation of TECPs at E- (top) and F-shell heights (bottom) on 11 June 2007 (DOY 162), along the line from northeast to southwest indicated as the red dashed line in Fig. 1. The black and gray dashed lines represent the occurrence time of perturbations and the alignment of evident downward-sloping stripes, respectively

Discussion

This study has simultaneously analyzed the night-time mid-latitude E- and F-region horizontal structuring and evolution when electrodynamic influenced irregularities (Es and MSTIDs) are present. According to the reconstructed results, irregularities aligned in NW–SE were simultaneously observed in E and F regions. Perkins instability and Es-layer instability are two mechanisms that can explain the tilted plasma density structures (Perkins 1973; Cosgrove and Tsunoda 2004). Previous simulation studies have found that the growth rate of the Perkins instability itself cannot account for the growth of typical MSTIDs, and the fastest growth of the coupled instability occurs when the unstable conditions on NW–SE perturbation are satisfied in both E and F regions (Yokoyama et al. 2008, 2009). Corroborating the earlier analyses and expositions on the morphology and dynamics in the coupling process obtained through observation and simulation (Hysell et al. 2004; Saito et al. 2007; Yokoyama et al. 2009; Liu et al. 2019), the E- and F-region irregularities are strongly coupled: the simultaneous irregularities in E and F regions share a similar wavefront (aligned from northwest to southeast), a common propagation direction (southwestward), and phase velocity (~100 m/s).

In Figs. 6 and 9, the Es structures on 23 June 2012 (DOY 175) (before 22:00 JST) and 11 June 2007 (DOY 162) have similar horizontal scales. However, the horizontal scale and intensity of MSTID structures in Fig. 9 are smaller than those in Fig. 6. This difference in MSTID structuring and development ought to depend on several factors that include the F-region background condition, the Es-layer intensity, and the duration of Es layer formation.

For MSTID event on 23 June 2012 (DOY 175), preexisting turbulences that cannot be captured by GNSS TEC have possibly perturbated the E (e.g., neutral wind shear) and F regions (e.g., gravity wave). In Fig. 8, the E- and F-region irregularities detected by GNSS TEC both develop after ~19:30 JST. However, the irregular structures in E and F regions reach the maximum amplitude at around 20:15 JST (~1.5 TECU) and 22:00 JST (~2 TECU), respectively. The much shorter time scale of the well-developed Es may be due to the thinner Es

layer, the larger growth rate of the Es-layer instability (Cosgrove and Tsunoda 2004), and the weak polarization electric fields from the F region (Cosgrove 2013). During 20:30–22:30 JST, the intensity of the Es layer reduced slightly, but the amplitude of F-region wave-like structures increase rapidly and reach the maximum. This fast development of irregularities in the F region could be attributed to the amplification of Perkins instability by large polarization electric fields via geomagnetic field lines, since the E-region irregularities determined by the double-shell approach have a typical horizontal scale of ∼150 km, which is able to produce polarization electric fields on this scale at night-time with more rapid onset of nonlinearity (Cosgrove 2013; Liu et al. 2019). At 22:15 JST, after the larger scale NW–SE structures are developed in the F region, the enhanced amplitude and elongated scale length of Es layer could result from the reinforced Es-layer courtesy of the polarization electric fields mapping from the F region (Yokoyama et al. 2009).

In a similar time period (∼19–24 JST) on 11 June 2007 (DOY 162), MSTID structures with smaller horizontal scale and intensity, and a similar duration of structure formation of Es and MSTIDs, were observed. Electrodynamics could be an explanation for the MSTID structures in this event, where the Es-layer instability plays a major role in seeding NW–SE irregularities in the F region (Cosgrove 2013). In Fig. 11, the evident downward-sloping stripes in the E region appear ∼10 min earlier, a time scale that agrees with the simulation results of the F-region response in the early stage of E–F coupling process (Cosgrove 2007; Yokoyama et al. 2009). As discussed in Sect. Event on DOY 162, 2007, the lower heights (< 300 km) of the F-region irregularities, which could be caused by the pole-ward neutral wind, can limit the instability structuring and amplitudes (Narayanan et al. 2014). In addition, the weaker Es layer (∼20% maximum amplitude decrease compared with 23 June 2012 (DOY 175)) on 11 June 2007 (DOY 162) can cause lower growth rate of the variation of the integrated Pedersen conductivity in the F region, which delays the development of MSTID structures (Yokoyama et al. 2009). Using GNSS TECPs with a double-thin-shell approach, the time scale of the full development of Es-layer structuring is about 160 min (from ∼18:50 to 21:30 JST), which is about 100 min larger than that on 23 June 2012 (DOY 175) (from ∼19:30 to 20:15 JST). Less sharp perturbation gradients in the E region on 11 June 2007 (DOY 162) produce smaller polarization electric fields associated with gradient drift instability (Cosgrove 2013), which can lead to the perturbation related to the Perkins instability tending to saturate at a smaller amplitude. Even so, the Es-layer instability still amplified the Perkins instability on 11 June 2007 (DOY 162): the time scale for producing large modulations in the F region has been shortened to about 1.5 h (from ∼19:00 to 20:30 JST) from 2 to 3 h (without an Es layer) (Cosgrove 2007). This mechanism could also be an explanation for the smaller intensity MSTIDs before sunrise on 23 June 2012 (DOY 175) in Fig. 8.

A complete understanding of the upper atmosphere electrodynamics is still a far-fetched idea that requires probing from different instrumentation on a larger spatial scale. The newly presented technique has attempted to partially fill this void by providing a broad horizontal scale and a high-resolution sneak view into the mid-latitude ionosphere E- and F-region during night irregularities; more important is that the deductions from the reconstructions have proved complementary to other types of observations.

Conclusions

In this paper, we used the perturbation components of TEC from ground-based GNSS observations to analyze the E–F coupling process by taking a double-thin-shell approach. TEC measurements were adopted from a densely distributed receiver network, GEONET, located over Japan with more than 1200 stations. The perturbation components of TEC in E and F regions were reconstructed on horizontal grids of 0.15° and 0.5°, respectively. Validation results from observation and simulation exhibited that the technique could reconstruct the irregularities in different layers with good fidelity. Two different event days of night-time MSTIDs on 23 June 2012 (DOY 175) and 11 June 2007 (DOY 162), were used to analyze the E–F coupling process. Consistent with the earlier analyses and expositions on the morphology and dynamics in the coupling process, the irregularities in E and F regions share a similar wavefront, propagation direction, and velocity. The F-region background condition, the Es-layer intensity, and the duration of Es layer formation could affect the development of MSTIDs, where the polarization electric fields play an important role. For the first time, the morphology and dynamics of the ionosphere perturbations in both E and F regions can be obtained simultaneously with ground-based GNSS TEC. Because the ground GNSS infrastructure is cost-effective and fast expanding, the research presented here is a vital step towards deepening our understanding of the generation mechanism of ionospheric irregularities: that is, to draw more patterns in E–F coupling, particularly in determining the actual drivers of the instabilities, a simultaneous run of the double-thin-shell model in geomagnetic conjugate hemispheres is feasible, in complement to other observational

campaigns previously hindered by constrained time budgets and high monitory run costs.

Abbreviations

DOY: Day of year; Es: Sporadic E; GNSS: Global Navigation Satellite System; IGRF: International geomagnetic reference field; IPP: Ionospheric piece point; JST: Japan Standard Time; MSTID: Medium-scale traveling ionospheric disturbance; MUR: Middle and upper atmosphere radar; QP echoes: Quasi-periodic echoes; RTI: Range-time-intensity; TEC: Total electron content; TECPs: TEC perturbations; UT: Universal time; 2-D: Two-dimensional; 3-D: Three-dimensional.

Supplementary Information

The online version contains supplementary material available at https://doi.org/10.1186/s40623-022-01639-w.

Additional file 1: Fig.S1. 2-D maps of input irregularities only in E shell (a–b), output irregularities (c–d), and corresponding residual distribution (e). 2-D maps of input irregularities only in F shell (f–g), output irregularities (h–i), and corresponding residual distribution (j).

Acknowledgements

This work was supported by JST SPRING Grant Number JPMJSP2110, and JSPS KAKENHI Grant Number JP20K04037.

Author contributions

FW conducted the research and prepared the manuscript. YT, SN, and LP contributed to the algorithm design and paper modification. YM supervised the project. All authors read and approved the final manuscript.

Funding

JST SPRING (JPMJSP2110) and JSPS KAKENHI (JP20K04037).

Availability of data and materials

The authors thank Geospatial Information Authority of Japan (GSI) for GEONET data at https://www.gsi.go.jp/ENGLISH/geonet_english.html, National Institute of Information and Communications Technology (NICT) for ionosonde data at https://wdc.nict.go.jp/IONO/, and for detrended TEC maps at https://aer-nc-web.nict.go.jp/GPS/DRAWING-TEC/, World Data Center for Geomagnetism for Dst data at http://wdc.kugi.kyoto-u.ac.jp/dstdir/index.html, Kakioka magnetic observatory for K index data at http://www.kakioka-jma.go.jp/obsdata/obsdata.html.

Declarations

Ethics approval and consent to participate

Not applicable.

Consent for publication

Not applicable.

Competing interests

The authors declare that they have no competing interests.

Author details

[1]Research Institute for Sustainable Humanosphere, Kyoto University, Uji, Kyoto 611-0011, Japan. [2]4DSpace, Department of Physics, University of Oslo, Blindern, 0316 Oslo, Norway.

Received: 31 January 2022 Accepted: 30 April 2022
Published online: 02 June 2022

References

Alken P, Thébault E, Beggan CD, Amit H, Aubert J, Baerenzung J, Zhou B (2021) International geomagnetic reference field: the thirteenth generation. Earth, Planets and Space 73(1):1–25. https://doi.org/10.1186/s40623-020-01288-x

Behnke R (1979) F layer height bands in the nocturnal ionosphere over Arecibo. J Geophys Res Space Physics 84(A3):974–978. https://doi.org/10.1029/JA084iA03p00974

Berkner LV, Wells HW (1934) F-region ionosphere-investigations at low latitudes. Terr Magn Atmos Electr 39(3):215–230. https://doi.org/10.1029/TE039i003p00215

Bowman GG (1985) Some aspects of mid-latitude spread-Es, and its relationship with spread-F. Planet Space Sci 33(9):1081–1089. https://doi.org/10.1016/0032-0633(85)90027-3

Bowman GG (1990) A review of some recent work on mid-latitude spread-F occurrence as detected by ionosondes. J Geomagn Geoelectr 42(2):109–138. https://doi.org/10.5636/jgg.42.109

Cosgrove RB (2007) Generation of mesoscale F layer structure and electric fields by the combined Perkins and Es layer instabilities, in simulations. Ann Geophys 25(7):1579–1601. https://doi.org/10.5194/angeo-25-1579-2007

Cosgrove R (2013) Mechanisms for E–F coupling and their manifestation. J Atmos Solar Terr Phys 103:56–65. https://doi.org/10.1016/j.jastp.2013.03.011

Cosgrove RB, Tsunoda RT (2004) Instability of the E–F coupled nighttime mid-latitude ionosphere. J Geophys Res Space Physics 109:A04305. https://doi.org/10.1029/2003JA010243

Farley DT Jr (1959) A theory of electrostatic fields in a horizontally stratified ionosphere subject to a vertical magnetic field. J Geophys Res 64(9):1225–1233. https://doi.org/10.1029/JZ064i009p01225

Fu W, Ssessanga N, Yokoyama T, Yamamoto M (2021) High-resolution 3-D imaging of daytime sporadic-E over Japan by using GNSS TEC and ionosondes. Space Weather. https://doi.org/10.1029/2021SW002878

Golub GH, Van Loan C (1989) Matrix computations. Johns Hopkins University Press, Baltimore

Haldoupis C, Kelley MC, Hussey GC, Shalimov S (2003) Role of unstable sporadic-E layers in the generation of midlatitude spread F. J Geophys Res Space Phys 108(A12):1446. https://doi.org/10.1029/2003JA009956

Haldoupis C, Meek C, Christakis N, Pancheva D, Bourdillon A (2006) Ionogram height–time–intensity observations of descending sporadic E layers at mid-latitude. J Atmos Solar Terr Phys 68(3–5):539–557. https://doi.org/10.1016/j.jastp.2005.03.020

Hernández-Pajares M, Juan JM, Sanz J (1999) New approaches in global ionospheric determination using ground GPS data. J Atmos Solar Terr Phys 61(16):1237–1247. https://doi.org/10.1016/S1364-6826(99)00054-1

Hunsucker RD (1982) Atmospheric gravity waves generated in the high-latitude ionosphere: a review. Rev Geophys 20(2):293–315. https://doi.org/10.1029/RG020i002p00293

Hysell DL, Larsen MF, Zhou QH (2004) Common volume coherent and incoherent scatter radar observations of mid-latitude sporadic E-layers and QP echoes. Ann Geophys 22(9):3277–3290. https://doi.org/10.5194/angeo-22-3277-2004

Hysell D, Larsen M, Fritts D, Laughman B, Sulzer M (2018) Major upwelling and overturning in the mid-latitude F region ionosphere. Nat Commun 9(1):1–11. https://doi.org/10.1038/s41467-018-05809-x

Kelley MC (2009) The Earth's ionosphere: plasma physics and electrodynamics. Academic Press, Cambridge

Larsen MF (2000) A shear instability seeding mechanism for quasiperiodic radar echoes. J Geophys Res Space Physics 105(A11):24931–24940. https://doi.org/10.1029/1999JA000290

Larsen MF (2002) Winds and shears in the mesosphere and lower thermosphere: results from four decades of chemical release wind measurements. J Geophys Res Space Phys. https://doi.org/10.1029/2001JA000218

Liu Y, Zhou C, Tang Q, Kong J, Gu X, Ni B, Yao Y, Zhao Z (2019) Evidence of mid-and low-latitude night-time ionospheric E–F coupling: coordinated observations of sporadic E Layers, F-region field-aligned irregularities, and medium-scale traveling ionospheric disturbances. IEEE Trans Geosci Remote Sens 57(10):7547–7557. https://doi.org/10.1109/TGRS.2019.2914059

Liu Y, Zhou C, Xu T, Wang Z, Tang Q, Deng Z, Chen G (2020) Investigation of midlatitude night-time ionospheric E–F coupling and interhemispheric coupling by using COSMIC GPS radio occultation measurements. J Geophys Res Space Phys 125(3):e2019JA027625. https://doi.org/10.1029/2019JA027625

Ma G, Maruyama T (2003) Derivation of TEC and estimation of instrumental biases from GEONET in Japan. Ann Geophys 21(10):2083–2093. https://doi.org/10.5194/angeo-21-2083-2003
Ma G, Gao W, Li J, Chen Y, Shen H (2014) Estimation of GPS instrumental biases from small scale network. Adv Space Res 54(5):871–882. https://doi.org/10.1016/j.asr.2013.01.008
Maeda J, Heki K (2014) Two-dimensional observations of midlatitude sporadic E irregularities with a dense GPS array in Japan. Radio Sci 49(1):28–35. https://doi.org/10.1002/2013RS005295
Maeda J, Heki K (2015) Morphology and dynamics of daytime mid-latitude sporadic-E patches revealed by GPS total electron content observations in Japan. Earth, Planets and Space 67(1):1–9. https://doi.org/10.1186/s40623-015-0257-4
Maruyama T, Fukao S, Yamamoto M (2000) A possible mechanism for echo striation generation of radar backscatter from midlatitude sporadic E. Radio Sci 35(5):1155–1164. https://doi.org/10.1029/1999RS002296
Maruyama T, Saito S, Yamamoto M, Fukao S (2006) Simultaneous observation of sporadic E with a rapid-run ionosonde and VHF coherent backscatter radar. Ann Geophys 24(1):153–162. https://doi.org/10.5194/angeo-24-153-2006
Maruyama T, Hozumi K, Ma G, Supnithi P, Tongkasem N, Wan Q (2021) Double-thin-shell approach to deriving total electron content from GNSS signals and implications for ionospheric dynamics near the magnetic equator. Earth, Planets and Space 73(1):1–21. https://doi.org/10.1186/s40623-021-01427-y
Mathews JD (1998) Sporadic E: current views and recent progress. J Atmos Solar Terr Phys 60(4):413–435. https://doi.org/10.1016/S1364-6826(97)00043-6
Mungufeni P, Kim YH, Ssessenga N (2021) Observations of ionospheric irregularities and its correspondence with sporadic e occurrence over South Korea and Japan. Adv Space Res 67(7):2207–2218. https://doi.org/10.1016/j.asr.2021.01.013
Narayanan VL, Shiokawa K, Otsuka Y, Saito S (2014) Airglow observations of night-time medium-scale traveling ionospheric disturbances from Yonaguni: statistical characteristics and low-latitude limit. J Geophys Res Space Physics 119:9268–9282. https://doi.org/10.1002/2014JA020368
Narayanan VL, Shiokawa K, Otsuka Y, Neudegg D (2018) On the role of thermospheric winds and sporadic E layers in the formation and evolution of electrified MSTIDs in geomagnetic conjugate regions. J Geophys Res Space Phys 123:6957–6980. https://doi.org/10.1029/2018JA025261
Nishioka M, Tsugawa T, Kubota M, Ishii M (2013) Concentric waves and short-period oscillations observed in the ionosphere after the 2013 Moore EF5 tornado. Geophys Res Lett 40(21):5581–5586. https://doi.org/10.1002/2013GL057963,2013
Otsuka Y, Tani T, Tsugawa T, Ogawa T, Saito A (2008) Statistical study of relationship between medium-scale traveling ionospheric disturbance and sporadic E layer activities in summer night over Japan. J Atmos Solar Terr Phys 70(17):2196–2202. https://doi.org/10.1016/j.jastp.2008.07.008
Otsuka Y, Shiokawa K, Ogawa T, Yokoyama T, Yamamoto M (2009) Spatial relationship of nighttime medium-scale traveling ionospheric disturbances and F region field-aligned irregularities observed with two spaced all-sky airglow imagers and the middle and upper atmosphere radar. J Geophys Res Space Phys 114:A05302. https://doi.org/10.1029/2008ja013902
Otsuka Y, Onoma F, Shiokawa K, Ogawa T, Yamamoto M, Fukao S (2007) Simultaneous observations of nighttime medium-scale traveling ionospheric disturbances and E region field-aligned irregularities at midlatitude. J Geophys Res Space Phys 112:A06317. https://doi.org/10.1029/2005JA011548
Otsuka, Y., Kotake, N., Shiokawa, K., Ogawa, T., Tsugawa, T., & Saito, A. (2011). Statistical study of medium-scale traveling ionospheric disturbances observed with a GPS receiver network in Japan. In Aeronomy of the Earth's Atmosphere and Ionosphere (pp. 291–299). Springer, Dordrecht. https://doi.org/10.1007/978-94-007-0326-1_21
Perkins F (1973) Spread F and ionospheric currents. J Geophys Res 78(1):218–226. https://doi.org/10.1029/JA078i001p00218
Saito A, Fukao S, Miyazaki S (1998) High resolution mapping of TEC perturbations with the GSI GPS network over Japan. Geophys Res Lett 25(16):3079–3082. https://doi.org/10.1029/98GL52361
Saito A, Nishimura M, Yamamoto M, Fukao S, Tsugawa T, Otsuka Y, Miyazaki S (2002) Observations of traveling ionospheric disturbances and 3-m scale irregularities in the night-time F-region ionosphere with the MU radar and a GPS network. Earth, Planets and Space 54(1):31–44. https://doi.org/10.1186/BF03352419
Saito S, Yamamoto M, Hashiguchi H, Maegawa A, Saito A (2007) Observational evidence of coupling between quasi-periodic echoes and medium scale traveling ionospheric disturbances. Ann Geophys 25(10):2185–2194. https://doi.org/10.5194/angeo-25-2185-2007
Saito S, Yamamoto M, Hashiguchi H (2008) Imaging observations of night-time mid-latitude F-region field-aligned irregularities by an MU radar ultra-multi-channel system. Ann Geophys 26(8):2345–2352. https://doi.org/10.5194/angeo-26-2345-2008
Shiokawa K, Ihara C, Otsuka Y, Ogawa T (2003) Statistical study of night-time medium-scale traveling ionospheric disturbances using midlatitude airglow images. J Geophys Res Space Phys 108(A1):1052. https://doi.org/10.1029/2002JA009491
Shukla AK, Das S, Nagori N, Sivaraman MR, Bandyopadhyay K (2009) Two-shell ionospheric model for Indian region: a novel approach. IEEE Trans Geosci Remote Sens 47(8):2407–2412. https://doi.org/10.1109/TGRS.2009.2017520
Sinno K, Ouchi C, Nemoto C (1964) Structure and movement of Es detected by LORAN observations. J Geomagn Geoelectr 16(2):75–88. https://doi.org/10.5636/jgg.16.75
Ssessanga N, Kim YH, Jeong S-H (2017) A statistical study on the F2 layer vertical variation during night-time medium-scale traveling ionospheric disturbances. J Geophys Res Space Phys 122(3):3586–3601. https://doi.org/10.1002/2016JA023463
Tsugawa T, Nishioka M, Ishii M, Hozumi K, Saito S, Shinbori A, Otsuka Y, Saito A, Buhari SM, Abdullah M, Supnithi P (2018) Total electron content observations by dense regional and worldwide international networks of GNSS. J Disaster Res 13(3):535–545. https://doi.org/10.20965/jdr.2018.p0535
Tsunoda RT (2006) On the coupling of layer instabilities in the night-time mid-latitude ionosphere. J Geophys Res Space Physics 111:A11304. https://doi.org/10.1029/2006JA011630
Tsunoda RT, Cosgrove RB (2001) Coupled electrodynamics in the night-time midlatitude ionosphere. Geophys Res Lett 28(22):4171–4174. https://doi.org/10.1029/2001GL013245
Whitehead JD (1989) Recent work on mid-latitude and equatorial sporadic-E. J Atmos Terr Phys 51(5):401–424. https://doi.org/10.1016/0021-9169(89)90122-0
Xie H, Li G, Zhao X, Ding F, Yan C, Yang G, Ning B (2020) Coupling between E region quasi-periodic echoes and F region medium-scale traveling ionospheric disturbances at low latitudes. J Geophys Res Space Phys 125(5):e2019JA027720. https://doi.org/10.1029/2019JA027720
Yamamoto M, Komoda N, Fukao S, Tsunoda RT, Ogawa T, Tsuda T (1994) Spatial structure of the E region field-aligned irregularities revealed by the MU radar. Radio Sci 29(1):337–347. https://doi.org/10.1029/93RS01846
Yang TY, Kwak YS, Kil H, Lee YS, Lee WK, Lee JJ (2015) Occurrence climatology of F region field-aligned irregularities in middle latitudes as observed by a 40.8 MHz coherent scatter radar in Daejeon, South Korea. J Geophys Res Space Phys 120(11):10107–10115. https://doi.org/10.1002/2015JA021885
Yokoyama T, Otsuka Y, Ogawa T, Yamamoto M, Hysell DL (2008) First three-dimensional simulation of the Perkins instability in the night-time midlatitude ionosphere. Geophys Res Lett 35:L03101. https://doi.org/10.1029/2007GL032496
Yokoyama T, Hysell DL, Otsuka Y, Yamamoto M (2009) Three-dimensional simulation of the coupled Perkins and Es-layer instabilities in the night-time midlatitude ionosphere. J Geophys Res Space Physics 114:A03308. https://doi.org/10.1029/2008JA013789
Zhou C, Tang Q, Huang F, Liu Y, Gu X, Lei J, Ni B, Zhao Z (2018) The simultaneous observations of night-time ionospheric E region irregularities and F region medium-scale traveling ionospheric disturbances in midlatitude China. J Geophys Res Space Physics 123(6):5195–5209. https://doi.org/10.1029/2018JA025352

Publisher's Note